Dielectric bi-layer model for electrochemical impedance spectroscopy characterisation of oxide film

Benoît Ter-Ovanessian, Jules Galipaud, Sabrina Marcelin, Bernard Tribollet, Bernard Normand

Dielectric bi-layer model for electrochemical impedance spectroscopy characterisation of oxide film

Benoît Ter-Ovanessian[a*], Jules Galipaud[a,b], Sabrina Marcelin[a], Bernard Tribollet[c]

Bernard Normand[a]

[a] *INSA Lyon, UCBL 1, CNRS, MATEIS, UMR5510, 69621 Villeurbanne, France*

[b] *Ecole Centrale de Lyon, CNRS, LTDS, UMR5513, 69130 Ecully, France*

[c] *Laboratoire Interfaces et Systèmes Electrochimiques (LISE), UMR 8235, CNRS-Sorbonne Université, Paris, France*

[*] Corresponding author. E-mail address: benoit.ter-ovanessian@insa-lyon.fr

Abstract

In this study, the impedance response of a passive material is investigated, attributing it to a normal time constant distribution caused by resistivity variations within the passive film. Two models, namely the Power Law Model (PLM) and the recently developed Dielectric Bi-Layer Model (DBLM), are employed to express the impedance data. The PLM considers an oxide film as a single layer with a power-law distribution of resistivity, while the DBLM incorporates two distinct layers: an inner layer with constant resistivity (ρ_0) and an outer layer with resistivity following Young's theory. Application of both models to 316L stainless steel immersed in a borate buffer solution exhibit that PLM and DBLM fitting results are in good agreement with experimental data. While the models differ mainly in resistivity profiles at the vicinity of the outer interface, the results suggest that deviations in regressed parameters indicate similar ranges for resistivity profiles calculated by both models. DBLM, in particular, is highlighted as promising for interpreting impedance data of passive materials due to its reliance on physical concepts.

Keywords: Electrochemical impedance spectroscopy, modelling, oxide film properties, passive behavior

1. Introduction

The formation of a dense, protective oxide layer on the surface of a metal is well accepted as one of the most scientifically and technologically relevant phenomenon for protecting materials against corrosion [1–4]. This aptitude provides a wide range of applications for metals without the need for any other corrosion protection. The understanding of the structure, properties and durability of this layer is therefore of paramount interest for corrosion engineering.

Many descriptive models such as the Point Defect Model (PDM) developed by MacDonald *et al.* [4–6] or Mixed Conduction Model (MCM) developed by Bojinov *et al*. [7–9] have been proposed to characterize the passive state. In the two cited models, passivation is characterized by various sequences of electrochemical reactions taking place at the metal/oxide and oxide/electrolyte interfaces, respectively, and is constrained by ionic or electronic transport within the oxide. For these models, the passive film primarily comprises one barrier layer. In MCM, the stoichiometric composition of this barrier layer gradually change across its thickness following the formal model of Young [10]. At the oxide/electrolyte interface, a hydrated and porous layer (generally called precipitated layer) is also identified, although in these cases, it is assumed that this layer does not significantly impact the electrical properties or electrochemical reactivity [4,6]. Alternatively, X-ray photoelectron spectroscopy (XPS) or time of flight secondary ions mass spectroscopy (ToF-SIMS) analyses reveal that the passive film is clearly not homogeneous in chemical composition throughout its thickness [11–14]. In the works of Marcus *et al.* [12–17] carried on stainless steels, the passive layer shows a compositional gradient. Closer to the metal, the oxide formed is rich in Cr while at the passive film/electrolyte interface, the enrichment is in Fe. In their calculation to estimate the thickness of the passive film, the authors assume a bi-layer model: a layer of pure Cr-oxide and a layer with the other oxides [14]. However, some major difficulties in validating this structure remain: (i) the passive film is a few nm in size, (ii) the depth of analysis is wider than the passive film thickness, (iii)

most surface analyses are done *ex-situ* while the hydrated layer is generally not stable in dry conditions, (iv) the abrading rate is depending on the local chemical composition. Furthermore, it is important to mention that the ToF-SIMS study shows that the change in composition is not abrupt and that there is a gradient zone [18]. Currently, it is still difficult to get information on the passive film structure and chemical analysis other than in an *ex-situ* approach. Only electrochemical measurements are prone to monitor the passive state, especially electrochemical impedance spectroscopy (EIS).

The impedance response typically obtained for studying a passive system is a truncated capacitive loop (usually associated with a large polarization resistance) [19–21]. The response of the passive film often deviates from an ideal capacitance. The graphical analysis of the phase corrected for the electrolyte resistance (proposed in [22]) easily evidences if a Constant Phase Element (CPE) or pseudo-CPE behavior could be associated with the impedance response of the considered passive film. A CPE is generally defined by two parameters the exponent α (adimensional) and the coefficient Q ($\mu F\ s^{(\alpha-1)}\ cm^{-2}$) which is related to the non-ideal capacitive behavior. On the frequency domain concerned, a constant phase below -90° indicates a pure CPE behavior while a pseudo-CPE behavior will correspond to a monotonic increase of the phase angle [21,23].

In both cases, it is possible to associate this deviation to the ideal capacitive behavior by a distribution of the resistivity along the film thickness [10,21,24,25]. On the one hand, Hirschorn *et al.*[26,27], based on mathematical considerations, propose the Power Law Model (PLM) attributing CPE behavior of the passive film to a power-law distribution of resistivity (ρ) along the passive film thickness (δ), given by:

$$\frac{\rho(\xi)}{\rho_\delta} = \left(\frac{\rho_\delta}{\rho_0} + \left(1 - \frac{\rho_\delta}{\rho_0}\right)\xi^\gamma\right)^{-1} \quad (1)$$

With

$$\gamma = \frac{1}{1-\alpha} \quad (2)$$

Where ρ_0 and ρ_δ are the limit resistivities at substrate/passive film and passive film/electrolyte interfaces, respectively, $\xi = x/\delta$ the non-dimensional thickness of the passive film with x the position normal to the surface (x=0 at metal/passive film interface). The resistivity profiles obtained from the data processing with PLM highlight two domains. At the vicinity of the metal surface, the resistivity is constant and equal to the resistivity ρ_0. This plateau is then followed by a decrease of the resistivity according to the power law. With this analysis, the dual character of the passive film is then taken into account. The inner layer can be attributed to the constant resistivity ρ_0 and the outer layer with the resistivity decay [20]. Several works [20,28,29] have highlighted the interest of this model for the characterization of the structure of passive films by studying, for example, the effect of polarization or alloying elements on the evolution of these profiles in Ni-based alloys or stainless steels. Nevertheless, it is important to mention that PLM is based on mathematical considerations and does not rely on a physical approach of the passive film. Moreover, the two layers of the passive film were considered with the same resistivity distribution law even though they are physico-chemically different.

On the other hand, the pseudo-CPE behavior is modeled by Young and would correspond to an evolution according to an exponential law of the resistivity [10,24]. In his physical approach, Young links this gradient to the non-stoichiometry of the oxide through the layer [10]. The distribution of the resistivity is given by:

$$\rho_{(x)} = \rho_0 \exp^{(-x/\lambda)} \quad (3)$$

Where ρ_0 is the limit resistivity at substrate/passive film, x is the position and λ is the characteristic length of the decay. The profiles obtained with Young's model take into account only one layer, the one with the decay and thus do not consider the possible dual character of the passive film. Thus, although the Young's model is based on physical concepts, it is only

valid for thick oxide or valve metals [10,21,23,30] and is not directly transposable to all passive layers. In addition, the MCM, mentioned previously, provides a physical basis for passive film based on the formal model of Young but considered a single oxide layer with a chemical composition gradient (defects concentration gradient) [7]. Thus presented, PLM and Young model generally used to describe the impedance of oxide films each present strengths and weaknesses for modeling passive films, with respect to physical considerations and surface analysis results.

In order to take into account the bi-layer character of passive film, it is then necessary to propose a model composed of a first homogeneous dielectric layer whose impedance model would be an ideal capacitance in parallel with a resistance and of a second layer corresponding to a modified layer which would be modeled by Young impedance. This model will be referenced as Dielectric Bi-Layer Model (DBLM). The originalities of this approach are, firstly the attribution of the CPE behavior observed on impedance response of passive film to the combination of R//C circuit associated with a Young impedance and secondly the evidence of the bi-layer character of the oxide through resistivity profile in agreement with the surface analysis considerations. The objective of this paper is thus to show the potentialities of this dielectric model composed of two layers to study oxide films, considering their physical and structural aspects. In a first part, the relationship between the CPE behavior, the PLM and the DBLM is established on theoretical impedance data. In a second part, the applicability of the assumptions of the proposed DBLM is discussed in the case of passivation of 316L stainless steel. The results of the parametric fits obtained with this latter model and with the PLM is compared. Regarding the obtained resistivity profiles, the bi-layer structure of the passive film is also investigated in detail by X-ray photoelectron spectroscopy (XPS).

2. Theoretical approach

Assuming that the passive film dielectric constant (ε) is constant in its thickness (δ), the PLM impedance of the passive film can be described by the integral [26,27]:

$$Z_{PLM}(\omega) = \delta \int_0^1 \frac{d\xi}{\rho_0^{-1} + j\omega\varepsilon\varepsilon_0 + (\rho_\delta^{-1} - \rho_0^{-1})\xi^\gamma} \quad (4)$$

With ε_0 the vacuum permittivity (8.85×10^{-14} F cm^{-1}) and ω the angular frequency ($\omega = 2\pi f$). According to the limit resistivity ρ_δ, the frequency domain of validity of the PLM is defined by characteristic frequencies f_δ calculated by:

$$f_\delta = \frac{1}{2\pi\varepsilon\varepsilon_0\rho_\delta} \quad (5)$$

For frequencies inferior to f_δ, the integrated expression of the PLM impedance can thus be written as follows:

$$Z_{PLM}(\omega) = g\frac{\delta\rho_\delta^{1-\alpha}}{(\rho_0^{-1} + j\omega\varepsilon\varepsilon_0)^\alpha} \quad (6)$$

where $g = 1 + 2.88(1-\alpha)^{2.375}$ (7)

From the PLM, the CPE parameter Q_{PLM} can be calculated by the following equation:

$$Q_{PLM} = \frac{(\varepsilon\varepsilon_0)^\alpha}{g\delta\rho_\delta^{1-\alpha}} \quad (8)$$

Conversely to PLM which is applicable on a certain frequency domain, Young impedance could be applied on the whole frequency range. In the Young model, an exponentially dependent resistivity and a relative dielectric constant independent of the position are assumed [10]. Consequently, the Young impedance is expressed as:

$$Z_Y(\omega) = -\frac{\lambda}{j\omega\varepsilon\varepsilon_0}\ln\left[\frac{1 + j\omega\varepsilon\varepsilon_0\rho_0 e^{(-\delta/\lambda)}}{1 + j\omega\varepsilon\varepsilon_0\rho_0}\right] \quad (9)$$

Where λ is the characteristic length of the decay.

As mentioned in the introduction part, both models exhibit some limitations. PLM should be used in a restricted frequency range and assume the same resistivity distribution law for the two layers while Young take into account one unique layer presenting the resistivity decay. In this work to originally account for the bi-layer feature of the passive film, the Young impedance, attributed to the outer layer, is associated in series with an ideal capacitance C_{in} in parallel with a resistance R_{in} standing for the inner layer features. The inner capacitance and the inner resistance are expressed as function of ρ_0 and δ_{in}, the thickness of the inner layer, as follows:

$$R_{in} = \rho_0 \delta_{in} \tag{10a}$$

and $$C_{in} = \frac{\varepsilon\varepsilon_0}{\delta_{in}} \tag{10b}$$

Then, the DBLM impedance is defined as:

$$Z_{DBLM}(\omega) = \frac{1}{\frac{j\omega\varepsilon\varepsilon_0}{\delta_{in}} + \frac{1}{\rho_0\delta_{in}}} - \frac{\lambda}{j\omega\varepsilon\varepsilon_0} \ln\left[\frac{1 + j\omega\varepsilon\varepsilon_0\rho_0 e^{\left(-\delta_{out}/\lambda\right)}}{1 + j\omega\varepsilon\varepsilon_0\rho_0}\right] \tag{11}$$

Where δ_{out} is the thickness of the outer layer.

The Electrical Equivalent Circuits (EECs) based on PLM or DBLM used to describe the oxidized metal/electrolyte interface are presented in Fig. 1.a and Fig. 1.b, respectively. In EEC1 (Fig.1.a) Z_{PLM} is the element corresponding to Eq. 6 used to describe the passive film response to the anodic non-faradaic branch while in EEC2 (Fig.1.b) R_{in} and C_{in} represents the inner part and Z_y the outer part of the passive layer. For both EECs, R_e represents the resistance of the electrolyte and C_{dl} is the capacitance of the electrochemical double layer at the oxide/electrolyte interface. The order of magnitude of the C_{dl} is generally ten times higher than the one of the passive film [31,32]. Consequently, as C_{dl} have a minor influence on the passive film properties, it was preferred to neglect it during the entire fitting process. R_{ct} is the charge-transfer resistance, which is attributed to the faradaic branch and generally to the cathodic reaction occurring at

passive film/electrolyte interface. In the case of anodic polarization, this resistance R_{ct} can be considered infinite because the cathodic reaction becomes negligible. $R_{ox,e}$ is the electronic resistance of the oxide correspond to the transfer of electrons generated at the electrolyte/oxide interface to the metal substrate. As those resistances (R_{ct} and $R_{ox,e}$) are in series, only the sum of the two can be determined [21].

3. Theoretical data

The applicability of the DBLM composed of a R//C circuit followed by the impedance of Young to characterize a CPE behavior relative to a PLM impedance is tested on 4 different sets of PLM parameters (δ, ρ_0, ρ_δ, α). These parameters were selected consistently with an oxide film/electrolyte interface and are reported in Table 1. The thickness is 3 nm (order of magnitude of passive films) and is fixed for the different data sets. The value of ρ_0 is also kept constant at 10^{13}. The value of α varies from 0.95 to 0.85 and the value of ρ_δ from 10^3 to 10^5. Only the last two parameters have been purposely modified in the datasets because they affect the shape of the resistivity profiles the most. The theoretical data were calculated from the Eq. 6 over a frequency range from 10^{-3} Hz to 10^4 Hz with 9 points per decade. The non-commercial regression program, SIMAD software developed at the LISE UMR 8235 CNRS, Sorbonne University, Paris, was used to calculate the PLM impedances resulting from each dataset (parameters on Table 1) and to regress the obtained impedance spectra with the DBLM (regressed parameters in Table 2). The regression method used in SIMAD is the Nelder–Mead method (also called downhill simplex method). This software is a fundamental input to impedance data analysis as it allows complex equations (*e.g.* electrochemical kinetics or impedance equations already mentioned above) to be written and impedance data to be fitted with different parameters.

Fig. 2.a shows the phase angle evolution as a function of the frequency (Bode diagram) for parameter set Data 1. The phase corrected by a R//C circuit (red star) is also displayed. In the

presence of pure CPE behavior, the phase is constant over the considered frequency range [22]. The α coefficient is directly accessible from the value of this phase angle according to [22]:

$$\varphi = -90 \times \alpha \quad (12)$$

The phase angle value here is 85°, corresponding to α of 0.95 over a wide frequency range. The second phase diagram presented on Fig. 2.a was obtained by subtracting from the data the impedance of a R//C circuit. Resistance and capacitance values were calculated from the resistivity profile obtained with the set Data 1 and shown on Fig. 2.b. The formula 10a and 10b were used with δ_{in} the length of the plateau observed on the resistivity profile and stand for the thickness of the inner layer. Here, R_{in} = 1.1 x10^6 Ω.cm² and C_{in}= 9.6 x10^{-6} µF.cm^{-2}. After correction (red star), it is interesting to note that the phase is no longer constant and increases monotonously from high to low frequencies. This evolution is often correlated with a pseudo-CPE behavior that can be modeled by Young impedance. Thus, this processing of the data confirms the benefit of using the DBLM model to simulate the PLM impedance.

As an example, Fig. 3 shows the Nyquist (Fig. 3.a) and Bode (Fig. 3.b) diagrams for parameter of the set Data 1. The curves resulting from the DBLM fit are also displayed. Agreement between the initial data and the fit data is tremendous. Fig. 3.b shows just a slight difference at high frequency between the two curves. This difference is discussed hereafter.

In addition, Table 2 reports the parameter values of the DBLM model when fitting impedance signal for each of the data sets detailed in Table 1. The sensitivity coefficient of the adjustment parameters is also indicated in percent. This coefficient is complementary to the χ parameter for fit optimization, and specifies the confidence with which the various fitting parameters must be considered. In this Table, the calculated values of δ_{tot}, R_{in}, C_{in} and $\rho_{\delta,calc}$ (which is the limit resistivity ρ_δ calculated by Eq. 3 with the regressed parameters) are also given for comparison. When the α value is close to 1 (Data 1 and Data 2), the results obtained by the DBLM model

are consistent with the initial parameter set, and the χ value is low. As α decreases, the difference between the initial and the fitted data increases. The most sensitive parameters are ρ_0 and δ_{in} which concern the high-frequency part of the model and also affect the obtained resistivity profile. Another point worth noting is the difference This trend is straightforwardly evidenced on the profile plots shown on Fig. 4. As already mentioned, the resistivity profile generated by PLM is characterized by a plateau for which the resistivity is equal to ρ_0 and a decay. For the DBLM, the plateau is related to the R//C contribution and the gradient to the Young impedance. Former part of the profile could be associated to the inner dense layer of the oxide and the latter to the outer defective layer.

For the sets Data 1 and Data 2 (Fig. 4.a and Fig. 4.b, respectively), the profiles obtained with PLM and DBLM are similar, excepted while approaching the outer layer/electrolyte interface where the limit resistivities exhibited few orders of magnitude difference. For the sets Data 3 and Data 4 (Fig. 4.c and Fig. 4.d, respectively), the resistivity profiles are in accordance for both models for the inner layer while they sharply deviate to the outer interface. The CPE exponent α stands for the dispersion of the time constants which vary according to the inhomogeneity through the oxide layer. If α value is too low, the passive layer might be considered a heterogenous layer with a property gradient which is not straightforwardly adjustable with the Young impedance. It is worth mentioning that, by definition, the contribution of the resistivities close to the passive film/electrolyte interface affects less the impedance response of the film than the highest resistivity part. To conclude, the results show that for α value superior to 0.9 (close to ideal capacitance behavior), the regressed data with DBLM are in agreement with theoretical PLM data, indicating that the substitution of PLM by DBLM is suitable. In the following part, both models are used on a practical case.

4. Application on 316L stainless steel in borate buffer solution

4.1 Experimental and data analysis procedures

Experiments were performed on a commercial 316L stainless steel sheet (referenced as 316L SS). The chemical composition of the austenitic stainless steel was: C (0.2 wt%), Si (0.49 wt%), S (0.001 wt%), P (0.035 wt%), Mn (1.79 wt%), Ni (10.1 wt%), Cr (16.7 wt%), Mo (2.03 wt%), balanced with Fe. Before the measurement, the specimen was ground with SiC paper down to 2400 and cleaned with ethanol and deionised water. The test solution was 0.05 M H_3BO_3 + 0.075 M $Na_2B_4O_7$ $10H_2O$ borate buffer solution (pH=9.2) open to air and maintained at 25 °C ± 2°C. This solution was selected because the solubility of the Cr-rich oxide or hydroxide is generally low for pH superior to 8 [33–35]. Consequently, the stability of the passive film grown on stainless steel is enhanced.

A recessed electrochemical cell was used for the electrochemical conditioning and EIS measurements. The main advantages of this geometry remain on the insurance of a uniform primary current distribution at the surface of the working electrode, resulting in the limitation of the frequency dispersion and imaginary contributions to Ohmic impedance which could be ideally modelled by a pure resistance [36]. A schematic representation of the used recessed electrochemical cell is displayed on Fig. 5. A K_2SO_4 saturated mercury/mercurous sulfate electrode (E_{MSE}= +0.658 V vs Standard Hydrogen Electrode at 25°C) and a graphite rod were used as reference and counter electrode, respectively. The distance between the counter/reference electrodes and the working electrode was fixed for all measurements and was larger than two times the diameter of the exposed surface of the working electrode. The exposed area was a disc of 1.5 cm^2. All the measurements were performed with electrochemical workstation SP-300 Potentiostat (Biologic, France) outfitted with ultra-low current module. EIS measurements were performed at open circuit potential (OCP) after 24h of immersion in the solution. The frequency range was from 10^5 Hz to 10^{-2} Hz with 9 points per decade and the

potential sinusoidal modulation amplitude was 15 mV. All the results and curves represented on the figures are representative to the average of three different measurements.

The impedance data were regressed using an open access software allowing measurement model analysis to remove the experimental data inconsistent with the Kramers-Kronig relations [37,38]. Then, the data were analyzed by a preliminary specific graphical analysis protocol [20,22,28] to determine the CPE parameters (α and Q) and the thickness of the passive layer. After the correction of the impedance response by the ohmic-resistance from electrolyte, the CPE behaviour could be evidenced and the CPE parameters could be determined graphically [22]. As previously shown (Eq. 11), α was estimated from ohmic-resistance corrected Bode plot. The coefficient of the CPE can be determined from Z'':

$$Q(\omega) = \sin\left(\frac{\alpha\pi}{2}\right)\frac{-1}{Z''\omega^{\alpha}} \quad (12)$$

This data processing and representation is a real asset for impedance data analysis, particularly at high frequencies in which the response of oxide films generally is. The thickness of the passive layer is determined by using the complex capacitance plane representation, obtained by plotting the imaginary part of the capacitance as a function of the real part of the capacitance obtained from the impedance signal corrected by the electrolyte resistance. This representation emphasizes values at high frequency, enabling determination of the high-frequency limit of the real part of the complex capacitance [21,39]. The high-frequency-limit capacitance here is related to the dielectric field within the passive film. This methodology was fully described and validated elsewhere [20,32,33,39]. Hence, the thickness of the passive film (δ) can be estimated from the capacitance from the complex representation (C_{HF}) using the formula:

$$\delta = \frac{\varepsilon\varepsilon_0}{C_{HF}}, \quad (13)$$

The graphically determined parameters provide some recommendation for the final regression of the impedance data. Fittings with SIMAD software by using EEC 1 with PLM (Eq. 6) and EEC 2 considering DBLM (Eq. 11) were separately done.

To discuss the bi-layer structure of the oxide film as proposed by the impedance data analysis, complementary surface analysis was performed on passive film grown during 24h on stainless steel in the borate buffered solution. XPS analysis was performed on a ULVAC-PHI Versaprobe 3 spectrometer using a monochromated AlKα source focused on the sample with a spot size of 200µm. All the selected transitions (Fe2p, Ni2p, Cr 2p, O1s, C1s) were recorded at a pass energy of 140 eV and alternated with argon ion bombardment accelerated at 500V during 30s steps. In these conditions, the etching rate was calibrated to a value of 0.004 nm s^{-1} on a silicon wafer with native oxide thickness of 1.2 nm. 75 cycles were recorded corresponding to 37.5 minutes of etching in total and according to the etch rate calibration 9 nm of sputtering depth. Spectra were fitted by separating the metallic and oxides + hydroxides contributions for each transition metal. In the case of Fe2p, only the Fe2p ½ signal was considered to avoid interference from Ni Auger signal. The extracted raw areas were then compared to the area of each contribution computed from a multilayer model presented below.

The multilayer model used in this work was build according to the procedure described in chapter 4 of [40]. For each sputter cycle, the intensity of each contribution was calculated taking into account the depth distribution of the different elements, the inelastic mean free path of the electrons involved, the ionization cross section, the transmission function of the apparatus. The assumptions that the sputter rate is constant through the layers and that the photon flux doesn't change significatively over the course of the whole experiment were made. A gaussian roughness factor was added at each interface to accommodate the experimental data.

4.2 EIS investigation of passive film grown on 316L stainless steel

Fig. 6 shows the impedance data obtained for 316L stainless steel samples after 24h of immersion at OCP in the borate buffer solution. Fig. 6.a, 6.b are the diagram plotted in the Nyquist coordinates. Fig. 6.b is a zoom in of Fig. 6.a to highlight the determination of the electrolyte resistance from the Nyquist plot at high frequencies. After checking the validity of the measurement by using measurement model [37,38], the impedance data measured at frequency lower than 0.1Hz were not considered consistent and not presented hereafter. In addition, the impedance data obtained for frequency higher than 10 kHz were not presented as the contribution to the measurement of the reference electrode artefact is not negligible in this frequency range.

The Nyquist diagram was characterized by a truncated capacitive loop, commonly observed for passive film. This result suggested that the resistance of polarization was very large and probably that the related charge transfer also. The electrolyte resistance was estimated at 107.9 ± 0.5 Ω cm^2. The experimental data were also plotted in a complex capacitance representation on Fig. 6.c to assess the capacitance value at infinite frequency. The C_{HF} value equal to 4.64 ± 0.60 µF cm^{-2} was related to a passive film thickness of 2.29 ± 0.26 nm (calculated by Eq. 13 with ε=12 for Cr_2O_3 [41]), which is consistent with the thickness generally obtained on stainless steel. Fig. 6.d and 6.e show the impedance data plotted in Bode coordinates. Results are plotted in ohmic-resistance corrected Bode plots. The straight line observed on the modulus vs log (f) is typical of the impedance response of a passive material. On the corrected phase shift, a clear plateau is evident between 5 Hz and 1200 Hz, which corresponds to a CPE behavior. Thus, the PLM may be used to analyze the data.

On Figs. 6.a, 6.d and 6.e the fitted curves considering EEC 1 and EEC 2 are also displayed. As noise on the measurement are observable on Figs. 6.b and 6.c at high frequencies above 1000 Hz, the experimental data were fitted on the frequency range 0.1 Hz to 1000 Hz. The possibility to regress within high frequencies is facilitated by the use of the recessed cell. For both EECs,

fitted and experimental curves are well-superimposed, especially on the modulus vs log (f) plot (Fig. 6.d). As discussed before slight differences are observed on the corrected phase shift (Fig. 6.e). The regressed parameters and their accuracy are reported on Table 3. As in the PLM, ρ_δ and δ appear in the numerator of the impedance function and are closely related, the regressed parameter *K* is used in SIMAD software. *K* is expressed as follow:

$$K = \delta \rho_\delta^{1-\alpha} \quad (14)$$

Then, ρ_δ is determined from *K* by inputting δ value assessed from Fig. 6.c and Eq. 13. From a general point of view, the low χ values for the two models used indicate that both regressions are satisfactory. The χ value of the regression using the DBLM slightly lower than for PLM. The order of magnitude of the resistivity ρ_0 at the metal/passive film interface was similar for both models, *ie.* 1-2 x10^{13} Ω cm and this value was generally observed for dense oxide layer [20,33,42]. Conversely, the value of the resistivity ρ_δ at passive film /electrolyte interface is ten times lower for DBLM than for PLM, accordingly to the decay law of resistivity *ie.* exponential law vs power law. Moreover, it is worth mentioning that the deviation on ρ_δ regressed with PLM is higher than that with DBLM.

Fig. 7 shows the resistivity profiles obtained from the fitted parameters given in Table 3 for both EECs. Dash lines represent the profiles accounting for the maximum deviations on ρ_0, ρ_δ, and δ/λ for both models. As previously observed on the theoretical data approach, the shape of the resistivity profiles obtained from both models is comparable. Notably the thickness of the inner layer of the passive film is similar, *ie.* close to 0.8 nm. Only differences on the resistivity profiles were locally observed at the passive film/electrolyte interface related to the used decay law. Considering the deviation of the regressed parameters, the enveloping curves of the mean profiles obtained by both models are superimposed in a wide range of thickness. Excepted at the close vicinity of the passive film/electrolyte interface, the resistivities determined by both

models are comparable within their respective deviations. From these results, it is difficult to conclude on the choice of the appropriate model or on the advantage of one over the other to characterize the passive film response.

As previously mentioned, the resistivity profile is comprised of two separate parts, suggesting the bi-layer structure of passive film in contact with electrolyte whatever the model used. From the alloy/passive film interface, the first part consisted of a plateau with ρ equal to ρ_0. This inner part exhibits almost an insulator behaviour with a homogeneous high resistivity. The second part considered the decay of the resistivity, reaching the passive film/solution interface resistivity ρ_δ. Here, the resistivity varies within the passive layer from the previous behaviour to a doped (disordered) semiconductor implying a significant evolution of composition or ionic and electronic defects concentration through this outer layer. In the present case, the DBLM seems more relevant than PLM as the exponential decay was associated to the non-stoichiometry of the oxide layer by Young theory [10]. Thus, the resistivity decrease is related to increasing stoichiometric deviation from the inner layer to the passive film/electrolyte interface due to lattice defects, interstitial cations but also substitution of cations in the main oxide network by other chemical species. Consequently, the proposed DBLM by assuming two distinct layers and considering physical approach should be preferentially used to model the duplex behavior of passive film grown on 316L stainless steel. It is also important to mention that the measurement or estimation of the thickness is not required for DBLM which is another advantage. Furthermore, by using DBLM, only one limit resistivity is regressed (ρ_0 or ρ_δ) and the other calculated by Eq. 3 while for PLM both of them are fitted. With the latter model, ρ_0 is difficulty estimated when the last measured frequency is superior to the characteristic frequency $f_0 = (2\pi\varepsilon\varepsilon_0\rho_0)^{-1}$ (see Eq. 6).

4.3 XPS analysis

To establish the relationship between the resistivity profiles obtained by PLM or DBLM with the chemistry of the passive layer, XPS analysis of passive film grown on 316L stainless steel in borate buffer solution after 24h of immersion was carried out using depth profiling at low Ar^+ energy (500 V).

Figs. 8.a, 8.b and 8.c illustrate the evolution of the spectra in the Fe2p, Cr2p and Ni2p regions, respectively, for sputtering durations ranging from 30 seconds to 2250 seconds. A basic PCA noise reduction employing four abstract factors was employed to enhance the signal-to-noise ratio. Metallic and oxidized states corresponding to respective binding energy peaks were detected from the first scan for the three regions. The evolutions of the peak intensity, shape and shift in binding energy were clearly observed for the three regions as the metal and oxide contributions change with the analysis depth. The lineshape of the spectra at the end of the sputtering procedure was taken as the pure metal contribution for the Cr2p and Ni2p regions. In the Fe2p region a best fit was found when considering some remaining oxidized species. These lineshapes were then applied to all intermediate spectra considering the remaining signal as oxidized species. No attempt at separating oxide and hydroxide contribution was made. Some examples of the decomposition and fitting of the spectra are shown in supplementary material (S1). From the fitted results, extracted raw areas for each contribution were then compared to the area computed from a multilayer model.

Fig. 9.a displays both the XPS raw area profiles (scatter plots) and the computed area from the model (solid lines) as a function of the etching depth for each XPS contribution while Fig. 9.b shows the corresponding atomic concentration at each depth extracted from the model. For an easier comparison with resistivity data, the x scale was set to 0 at the interface between metal film and passive film. The parameters of interest of the model are summarized in Table 4.

The model parameters (layer thickness, roughness, density and composition) were selected to match as best as possible the raw areas extracted from XPS. The best fit is obtained when proposing a multilayer system composed of a contamination layer exclusively composed of carbon on the top (3.1<x<3.3 nm), two oxide-rich layers (0<x<3.1 nm) and two metal rich layers beneath (-4.0<x<0 nm). The bulk layer has a composition of 74.8 at% Fe 14.4 at% Cr and 11.8 at% Ni which is close to the known bulk composition of 316L stainless steel. This composition combined with a density of 8 g cm^{-3} was used as a reference to calculate the other elements semi-infinite intensities, needed to compute the areas extracted from the model. A remaining signal of oxygen and iron oxide is still present in the experimental data probably due to the ion bombardment that either generate redeposition of sputtered material on the surface, or does not completely remove some surface material from the XPS area of analysis.

An interfacial metallic layer comes directly on top of the bulk layer and is very similar to it. It accounts for a small increase from 11.8 to 15 at% of Ni compared to the bulk. This phenomenon is well known in such steel surfaces [12,43] and is explained by preferential oxidation of chromium and segregation of nickel away from the top surface and down deeper at the interface between the passive film and the bulk metal. The oxygen rich film is set on top of the interfacial layer and is mainly formed of chromium, iron and oxygen. It corresponds to the passive bi-layer under investigation in this study.

As XPS clearly shows, two layers with different compositions can be isolated. While the inner layer is composed of a mixture of chromium and iron oxide/hydroxide, the outer layer is almost exclusively composed of iron oxide and hydroxide species. This result is in line with the studied models for impedance data analysis that consider two dielectric layers: a layer with homogenous resistivity and a layer with a resistivity decay. A last layer composed of carbon accounts for the contamination of the surface and explains a decrease of the Fe and O intensities at the top surface. The oxygen content (59 at%) in the inner layer matches the hypothesis of a

mixed oxide (Cr_2O_3, Fe_2O_3) layer (oxygen to metal ratio of 1.5), the outer layer displays an oxygen to metal ratio of 2 that is higher and could be the sign of non-stochiometric oxide or the presence of hydroxide species.

Comparison of the thickness of inner and outer layers of passive film with the EIS data shows some differences, especially comparing the ratio of thicknesses. While in the XPS model, the two layers have similar thickness. EIS data shows that the inner layer is two times smaller than the outer layer. A few hypotheses can be put forward to discuss this difference. First in the XPS data, a constant etch rate was considered which can lead to inaccuracies in the absolute determination of the thickness but can also induce distortion within the different layers. The etch rate being sensitive to the density and composition of the material. If the etch rate is different in both layers, it is likely that the presented calculation has underestimated the thickness of outer layer and overestimated the thickness of inner layer which goes in the right direction to match the EIS data. Moreover, it has to be noted that while EIS is performed *in situ*, XPS is performed *ex situ* and the sample has to be analyzed under ultra-high-vacuum. This can lead to a modification of the water rich outer layer as shown by Yue *et al.* [44] who performed Near-Ambient-Pressure-XPS measurements on passive films under synchrotron radiation.

Finally, the duplex structure of passive film could be defined by XPS analysis in the case of 316L stainless steel indicating that the previous EIS data analysis by DBLM or PLM are appropriate to model the passive film. Even if this structure is considered while resistivity profile is obtained from PLM parameters, the DBLM presents the benefit to assume two distinct layers with two different chemical composition and electronic properties as described by XPS analysis: the inner layer which is a mixed oxide (Cr_2O_3, Fe_2O_3) enriched in Cr and the outer layer which is enriched in Fe and in hydroxide groups. This finding is straightforwardly consistent with the multi-layer model of the attenuation of the emitted photoelectrons as proposed by XPS analysis.

5. Conclusions

The objectives of this work were to accurately study by a dedicated methodology the impedance response of a passive material in contact with an electrolyte and to compare two models considering that the impedance response of the passive film be attributed to a normal time constant distribution caused by resistivity variations through its thickness: Power Law Model (PLM) and the proposed Dielectric Bi-Layer Model (DBLM).

In this work, the recessed cell was used to limit the contribution of the ohmic impedance to a pure resistance. The validity of the data and the accurate range of analyzed frequency were checked by the measurement model. It is worth mentioning that measuring a large number of frequencies per decade, is also important to enhance the quality of the analysis. Then, the advanced graphical analysis was used allowing to determine different parameters. This methodological step provides information for the selection of the regression model. In the present case, the value of α may prescribe the use of PLM or DBLM. As observed in the theoretical part, the applicability of the latter seems relevant for high value of α. Furthermore, it is also imperative to mention the hypotheses done during the analysis. For example, the double layer capacitance was neglected as the data analysis was mainly focused on high frequency response but it could be interesting to consider it for certain practical cases.

In the case study of 316L, the resistivity profiles and the fitted parameters obtained by both models were similar and in good agreement with the experimental data, indicating that they are both adapted to interpret the impedance of dielectric oxide layer. PLM is a mathematical model which necessitate the determination of the passive film thickness by another method (complex-capacitance analysis or XPS). Conversely, the major advantages of DBLM are: (i) it assumes two distinct layers, (ii) Young's resistivity distribution within the outer layer is based on physical

considerations, (iii) the regression with DBLM relies on few unknown parameters and the adjustment of certain parameters (limit resistivity at interface ρ_0 or ρ_δ and oxide layer thickness *δ)* is facilitated with an enhanced precision conversely to PLM. The duplex description proposed in this work by both models is consistent with surface analysis approach: an inner oxide layer, rather homogenous in chemical composition with limited defect content with high resistivity and an outer oxide layer presenting a chemical gradient as well as a gradient in defects concentration (resulting in resistivity variation).

CRediT authorship contribution statement

Benoît Ter-Ovanessian: Conceptualization, Data curation, Investigation, Methodology, Writing – original draft, Writing – review & editing. **Jules Galipaud:** Data curation, Investigation, Methodology, Writing – original draft, Writing – review & editing. **Sabrina Marcelin:** Conceptualization, Methodology, Writing – original draft, Writing – review & editing. **Bernard Tribollet:** Conceptualization, Methodology, Supervision, Writing – original draft, Writing – review & editing. **Bernard Normand:** Conceptualization, Supervision, Writing – review & editing**.**

Declaration of competing interest

The authors declare no conflict of interests.

Data availability

The raw/processed data required to reproduce these findings cannot be shared at this time as the data also forms part of an ongoing study.

References

[1] N. Sato, An overview on the passivity of metals, Corros. Sci. 31 (1990) 1–19. https://doi.org/10.1016/0010-938X(90)90086-K.
[2] P. Schmuki, From Bacon to barriers: a review on the passivity of metals and alloys, J. Solid State Electrochem. 6 (2002) 145–164. https://doi.org/10.1007/s100080100219.
[3] H.-H. Strehblow, Passivity of Metals Studied by Surface Analytical Methods, a Review, Electrochimica Acta 212 (2016) 630–648. https://doi.org/10.1016/j.electacta.2016.06.170.
[4] D.D. Macdonald, The history of the Point Defect Model for the passive state: A brief review of film growth aspects, Electrochimica Acta 56 (2011) 1761–1772. https://doi.org/10.1016/j.electacta.2010.11.005.
[5] D. Macdonald, G. Englehardt, The Point Defect Model for Bi-Layer Passive Films, ECS Trans. 28 (2010) 123–144. https://doi.org/10.1149/1.3496427.
[6] D.D. Macdonald, M. Urquidi-Macdonald, Theory of Steady-State Passive Films, J. Electrochem. Soc. 137 (1990) 2395–2402. https://doi.org/10.1149/1.2086949.
[7] M. Bojinov, G. Fabricius, P. Kinnunen, T. Laitinen, K. Mäkelä, T. Saario, G. Sundholm, Electrochemical study of the passive behaviour of Ni–Cr alloys in a borate solution—a mixed-conduction model approach, J. Electroanal. Chem. 504 (2001) 29–44. https://doi.org/10.1016/S0022-0728(01)00423-5.
[8] M. Bojinov, G. Fabricius, T. Laitinen, K. Mäkelä, T. Saario, G. Sundholm, Coupling between ionic defect structure and electronic conduction in passive films on iron, chromium and iron–chromium alloys, Electrochimica Acta 45 (2000) 2029–2048. https://doi.org/10.1016/S0013-4686(99)00423-5.
[9] I. Betova, M. Bojinov, V. Karastoyanov, P. Kinnunen, T. Saario, Estimation of kinetic and transport parameters by quantitative evaluation of EIS and XPS data, Electrochimica Acta 55 (2010) 6163–6173. https://doi.org/10.1016/j.electacta.2009.11.100.
[10] L. Young, Anodic oxide films. Part 4.—The interpretation of impedance measurements on oxide coated electrodes on niobium, Trans. Faraday Soc. 51 (1955) 1250–1260. https://doi.org/10.1039/TF9555101250.
[11] A. Barroux, T. Duguet, N. Ducommun, E. Nivet, J. Delgado, L. Laffont, C. Blanc, Combined XPS / TEM study of the chemical composition and structure of the passive film formed on additive manufactured 17-4PH stainless steel, Surf. Interfaces 22 (2021) 100874. https://doi.org/10.1016/j.surfin.2020.100874.
[12] B. Lynch, S. Neupane, F. Wiame, A. Seyeux, V. Maurice, P. Marcus, An XPS and ToF-SIMS study of the passive film formed on a model FeCrNiMo stainless steel surface in aqueous media after thermal pre-oxidation at ultra-low oxygen pressure, Appl. Surf. Sci. 554 (2021) 149435. https://doi.org/10.1016/j.apsusc.2021.149435.
[13] X. Wang, D. Mercier, S. Zanna, A. Seyeux, L. Perriere, M. Laurent-Brocq, I. Guillot, V. Maurice, P. Marcus, XPS study of the thermal stability of passivated NiCrFeCoMo multi-principal element alloy surfaces, Surf. Interface Anal. 55 (2023) 457–465. https://doi.org/10.1002/sia.7193.
[14] L. Wang, A. Seyeux, P. Marcus, Thermal stability of the passive film formed on 316L stainless steel surface studied by ToF-SIMS, Corros. Sci. 165 (2020) 108395. https://doi.org/10.1016/j.corsci.2019.108395.
[15] E. Gardin, S. Zanna, A. Seyeux, A. Allion-Maurer, P. Marcus, Comparative study of the surface oxide films on lean duplex and corresponding single phase stainless steels by XPS and ToF-SIMS, Corros. Sci. 143 (2018) 403–413. https://doi.org/10.1016/j.corsci.2018.08.009.
[16] B. Lynch, F. Wiame, V. Maurice, P. Marcus, XPS study of oxide nucleation and growth mechanisms on a model FeCrNiMo stainless steel surface, Appl. Surf. Sci. 575 (2022) 151681. https://doi.org/10.1016/j.apsusc.2021.151681.

[17] Z. Wang, F. Di-Franco, A. Seyeux, S. Zanna, V. Maurice, P. Marcus, Passivation-Induced Physicochemical Alterations of the Native Surface Oxide Film on 316L Austenitic Stainless Steel, J. Electrochem. Soc. 166 (2019) C3376. https://doi.org/10.1149/2.0321911jes.
[18] E. Gardin, S. Zanna, A. Seyeux, A. Allion-Maurer, P. Marcus, XPS and ToF-SIMS characterization of the surface oxides on lean duplex stainless steel – Global and local approaches, Corros. Sci. 155 (2019) 121–133. https://doi.org/10.1016/j.corsci.2019.04.039.
[19] M. Santamaria, F.D. Franco, F.D. Quarto, M. Pisarek, S. Zanna, P. Marcus, Photoelectrochemical and XPS characterisation of oxide layers on 316L stainless steel grown in high-temperature water, J. Solid State Electrochem. (2015) 1–9. https://doi.org/10.1007/s10008-015-2849-0.
[20] S. Marcelin, Z. Zhang, B. Ter-Ovanessian, B. Normand, Relationship between the Resistivity Profiles Obtained from the Power Law Model and the Physico-Chemical Properties of Passive Films, J. Electrochem. Soc. 168 (2021) 021503. https://doi.org/10.1149/1945-7111/abde84.
[21] B. Tribollet, V. Vivier, M.E. Orazem, EIS Technique in Passivity Studies: Determination of the Dielectric Properties of Passive Films, in: K. Wandelt (Ed.), Ref. Module Chem. Mol. Sci. Chem. Eng., Elsevier, 2017. https://doi.org/10.1016/B978-0-12-409547-2.13817-X.
[22] M.E. Orazem, N. Pébère, B. Tribollet, Enhanced Graphical Representation of Electrochemical Impedance Data, J. Electrochem. Soc. 153 (2006) B129–B136. https://doi.org/10.1149/1.2168377.
[23] I. Frateur, Characterization of Oxide Films by Electrochemical Impedance, ECS Trans. 13 (2008) 115–128. https://doi.org/10.1149/1.3004033.
[24] P. Córdoba-Torres, A generalized expression for the resistivity distribution in films: from the Young model to constant-phase element (CPE) behavior, Electrochimica Acta (2017). https://doi.org/10.1016/j.electacta.2017.04.147.
[25] M.E. Orazem, I. Frateur, B. Tribollet, V. Vivier, S. Marcelin, N. Pébère, A.L. Bunge, E.A. White, D.P. Riemer, M. Musiani, Dielectric Properties of Materials Showing Constant-Phase-Element (CPE) Impedance Response, J. Electrochem. Soc. 160 (2013) C215–C225. https://doi.org/10.1149/2.033306jes.
[26] B. Hirschorn, M.E. Orazem, B. Tribollet, V. Vivier, I. Frateur, M. Musiani, Determination of effective capacitance and film thickness from constant-phase-element parameters, Electrochimica Acta 55 (2010) 6218–6227. https://doi.org/10.1016/j.electacta.2009.10.065.
[27] B. Hirschorn, M.E. Orazem, B. Tribollet, V. Vivier, I. Frateur, M. Musiani, Constant-Phase-Element Behavior Caused by Resistivity Distributions in Films: II. Applications, J. Electrochem. Soc. 157 (2010) C458. https://doi.org/10.1149/1.3499565.
[28] Z. Zhang, B. Ter-Ovanessian, S. Marcelin, B. Normand, Investigation of the passive behavior of a Ni–Cr binary alloy using successive electrochemical impedance measurements, Electrochimica Acta 353 (2020) 136531. https://doi.org/10.1016/j.electacta.2020.136531.
[29] Z. Zhang, B. Ter-Ovanessian, S. Marcelin, J. Galipaud, B. Normand, Role of Alloying Elements in Passive and Transpassive Behavior of Ni–Cr-Based Alloys in Borate Buffer Solution, J. Electrochem. Soc. 168 (2021) 081503. https://doi.org/10.1149/1945-7111/ac1890.
[30] C.J. Dell'oca, D.L. Pulfrey, L. Young, Anodic Oxide Films, in: M.H. Francombe, R.W. Hoffman (Eds.), Phys. Thin Films, Elsevier, 1971: pp. 1–79. https://doi.org/10.1016/B978-0-12-533006-0.50008-6.

[31] S. Chakri, I. Frateur, M.E. Orazem, E.M.M. Sutter, T.T.M. Tran, B. Tribollet, V. Vivier, Improved EIS Analysis of the Electrochemical Behaviour of Carbon Steel in Alkaline Solution, Electrochimica Acta 246 (2017) 924–930. https://doi.org/10.1016/j.electacta.2017.06.096.
[32] V. Vivier, O. Gharbi, M. Tran, M. Orazem, M. Turmine, B. Tribollet, impedance response of a thin film on an electrode: Deciphering the influence of the double layer capacitance, Chemphyschem Eur. J. Chem. Phys. Phys. Chem. (2021). https://doi.org/10.1002/cphc.202100177.
[33] S.EL. Euch, D. Bricault, H. Cachet, E.M.M. Sutter, M.T.T. Tran, V. Vivier, N. Engler, A. Marion, M. Skocic, B. Huerta-Ortega, Temperature dependence of the electrochemical behavior of the 690 Ni-base alloy between 25 and 325 °C, Electrochimica Acta 317 (2019) 509–520. https://doi.org/10.1016/j.electacta.2019.05.131.
[34] V. Jovancicevic, P. Zelenay, B.R. Scharifker, The transport properties of oxygen in aqueous borate solutions, Electrochimica Acta 32 (1987) 1553–1555. https://doi.org/10.1016/0013-4686(87)90002-8.
[35] D. Rai, B.M. Sass, D.A. Moore, Chromium(III) hydrolysis constants and solubility of chromium(III) hydroxide, Inorg. Chem. 26 (1987) 345–349. https://doi.org/10.1021/ic00250a002.
[36] I. Frateur, V.M.-W. Huang, M.E. Orazem, N. Pébère, B. Tribollet, V. Vivier, Local electrochemical impedance spectroscopy: Considerations about the cell geometry, Electrochimica Acta 53 (2008) 7386–7395. https://doi.org/10.1016/j.electacta.2008.01.012.
[37] P. Agarwal, M.E. Orazem, L.H. Garcia-Rubio, Application of Measurement Models to Impedance Spectroscopy: III . Evaluation of Consistency with the Kramers-Kronig Relations, J. Electrochem. Soc. 142 (1995) 4159. https://doi.org/10.1149/1.2048479.
[38] M.E. Orazem, Measurement model for analysis of electrochemical impedance data, J. Solid State Electrochem. (2023). https://doi.org/10.1007/s10008-023-05755-9.
[39] M. Benoit, C. Bataillon, B. Gwinner, F. Miserque, M.E. Orazem, C.M. Sánchez-Sánchez, B. Tribollet, V. Vivier, Comparison of different methods for measuring the passive film thickness on metals, Electrochimica Acta (2016). https://doi.org/10.1016/j.electacta.2015.12.173.
[40] J.E. Castle, Practical surface analysis by Auger and X-ray photoelectron spectroscopy. D. Briggs and M. P. Seah (Editors). John Wiley and Sons Ltd, Chichester, 1983, 533 pp., £44.50, Surf. Interface Anal. 6 (1984) 302–302. https://doi.org/10.1002/sia.740060611.
[41] B. Lovreček, J. Sefaja, Semiconducting aspects of the passive layer on chromium, Electrochimica Acta 17 (1972) 1151–1155. https://doi.org/10.1016/0013-4686(72)90031-X.
[42] C. Nkoua, J. Esvan, B. Tribollet, R. Basseguy, C. Blanc, Combined electrochemical impedance spectroscopy and X-ray photoelectron spectroscopy analysis of the passive films formed on 5083 aluminium alloy, Corros. Sci. 221 (2023) 111337. https://doi.org/10.1016/j.corsci.2023.111337.
[43] W. Fredriksson, S. Malmgren, T. Gustafsson, M. Gorgoi, K. Edström, Full depth profile of passive films on 316L stainless steel based on high resolution HAXPES in combination with ARXPS, Appl. Surf. Sci. 258 (2012) 5790–5797. https://doi.org/10.1016/j.apsusc.2012.02.099.
[44] X. Yue, A. Larsson, H. Tang, A. Grespi, M. Scardamaglia, A. Shavorskiy, A. Krishnan, E. Lundgren, J. Pan, Synchrotron-based near ambient-pressure X-ray photoelectron spectroscopy and electrochemical studies of passivation behavior of N- and V-

containing martensitic stainless steel, Corros. Sci. 214 (2023) 111018. https://doi.org/10.1016/j.corsci.2023.111018.

Figure captions:

Figure 1. *Electrical Equivalent circuits used to fit data response of metal/passive film/electrolyte interfaces: a) EEC1 using PLM; b) EEC2 using DBLM.*

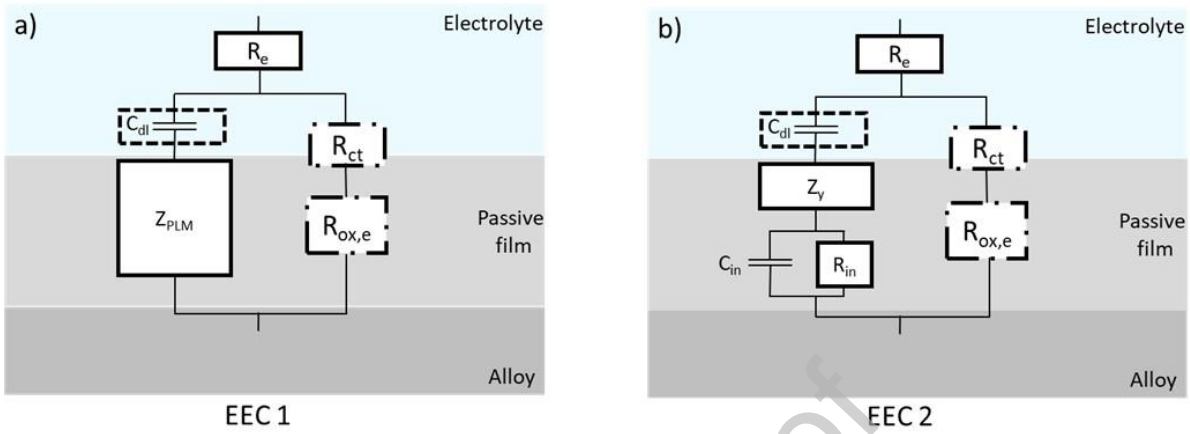

Figure 2. *Phase and corrected by R//C phase diagrams from the impedance response of theoretical Data 1(a) and the resistivity profile obtained (Eq. 1) with the same dataset (b).*

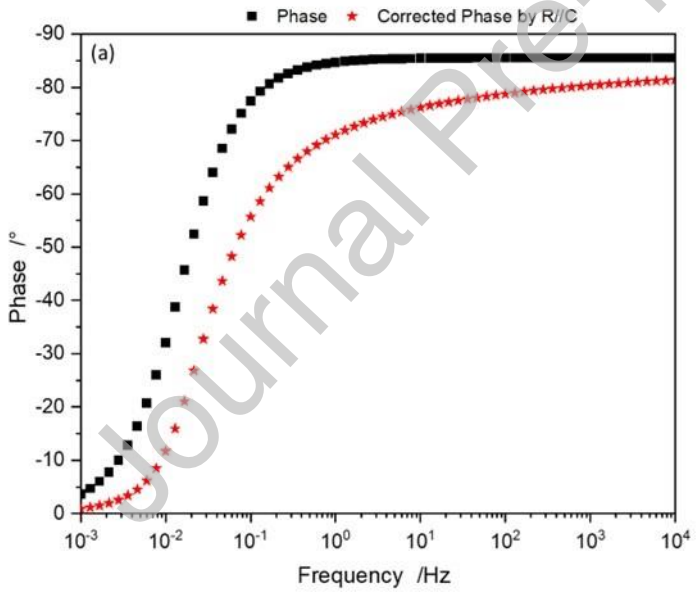

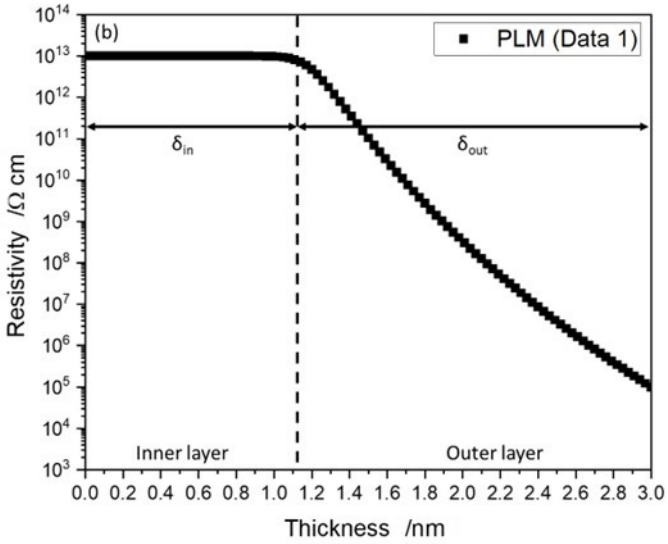

Figure 3. *Impedance results of theoretical data 1 and regression results with equivalent electrical circuit 2: a) Nyquist plot; b) Bode plot.*

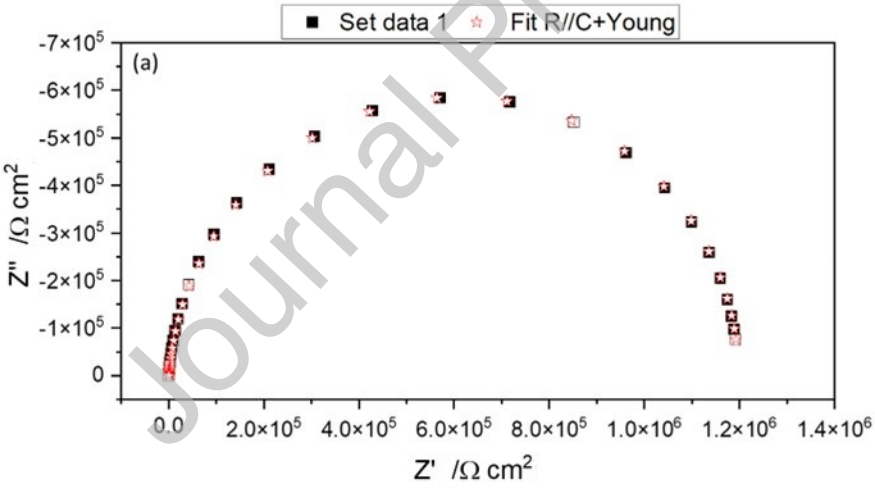

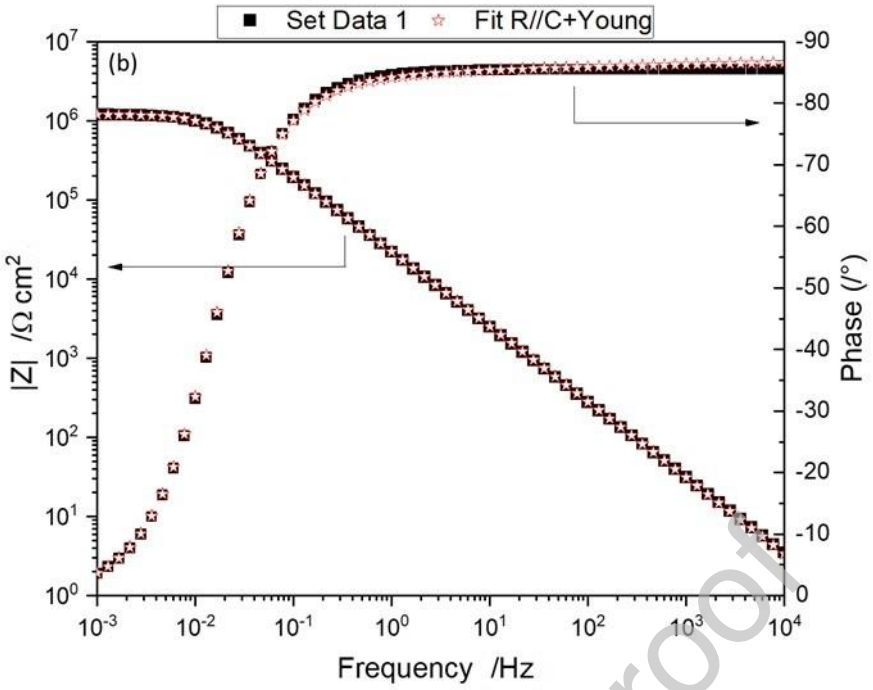

Figure 4. *Resistivity profiles obtained for the four data sets following the PLM or DBLM (R//C+Young): a) Data 1, b) Data 2, c) Data 3, d) Data 4*

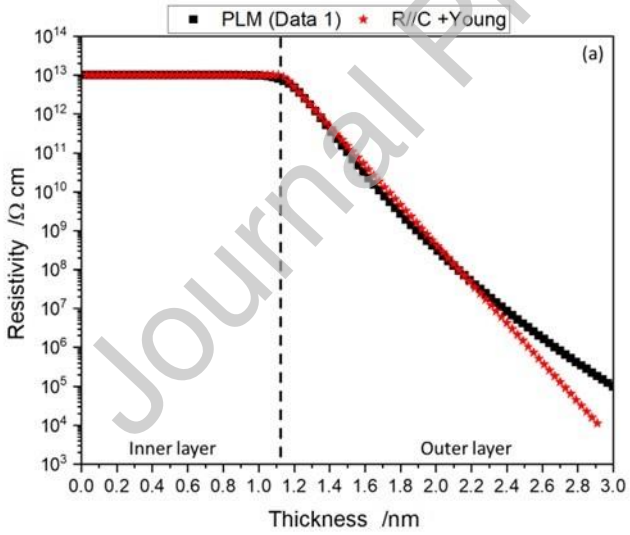

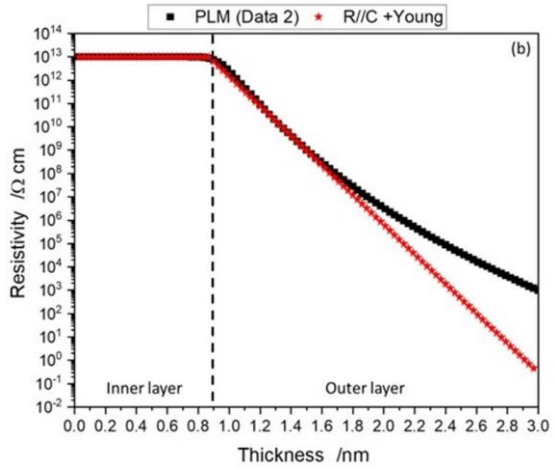

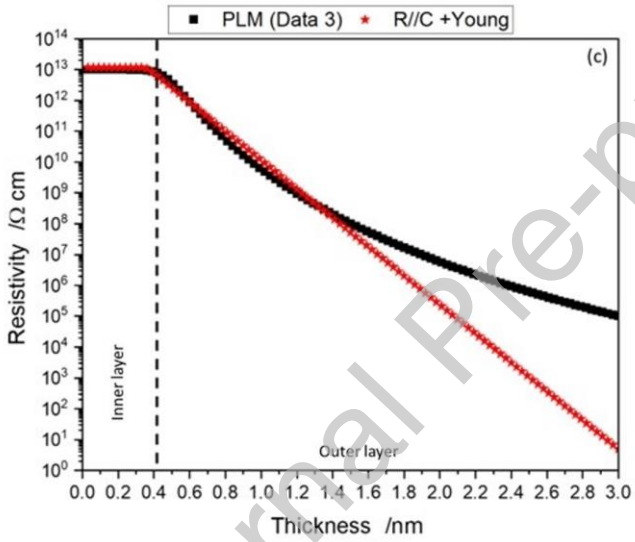

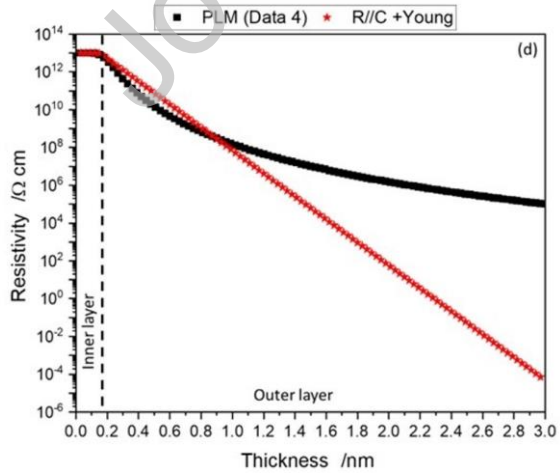

Figure 5. *Schematic representation of the recessed electrochemical cell. r is the radius of the exposed surface of the working electrode and L the recess depth (L>2r).*

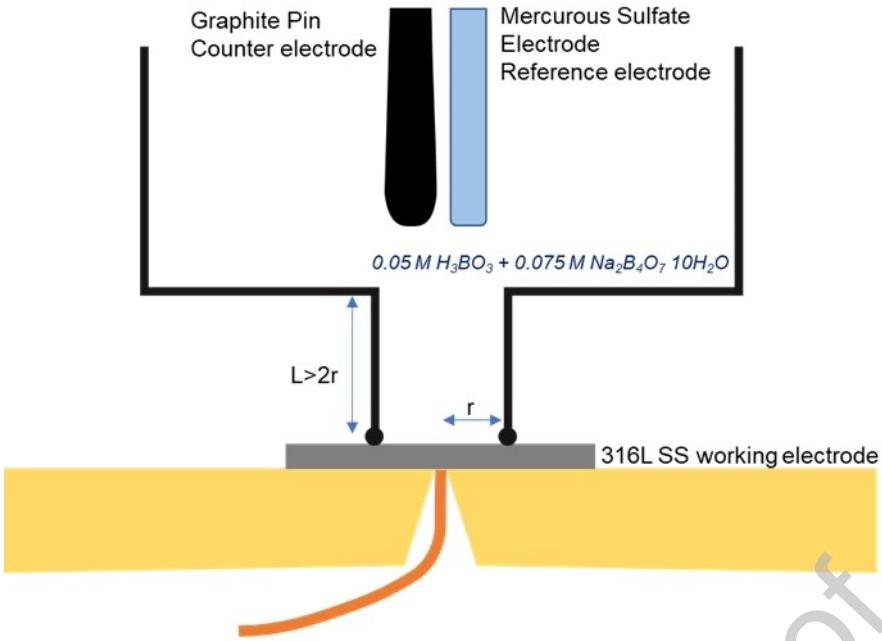

Figure 6. *Impedance response for 316L stainless steel after 24h in aerated 0.05 M H_3BO_3 + 0.075 M $Na_2B_4O_7$ 10H_2O borate buffer solution (pH=9.2): a) Nyquist plot; b) detail of the Nyquist plot for electrolyte resistance determination; c) complex capacitance representation for infinite capacitance determination; d) corrected modulus as a function of frequency; e) corrected phase as a function of frequency.*

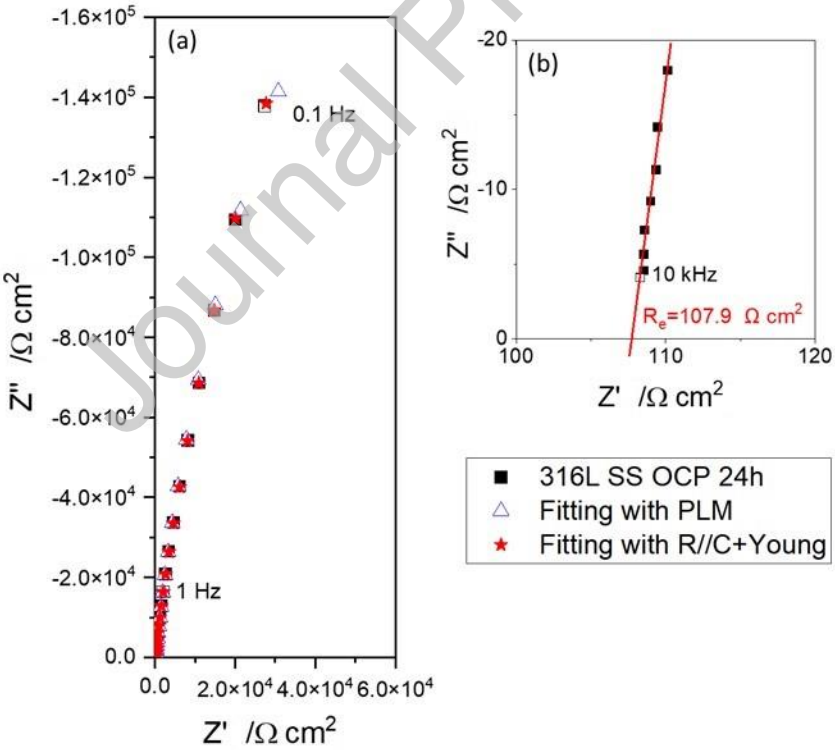

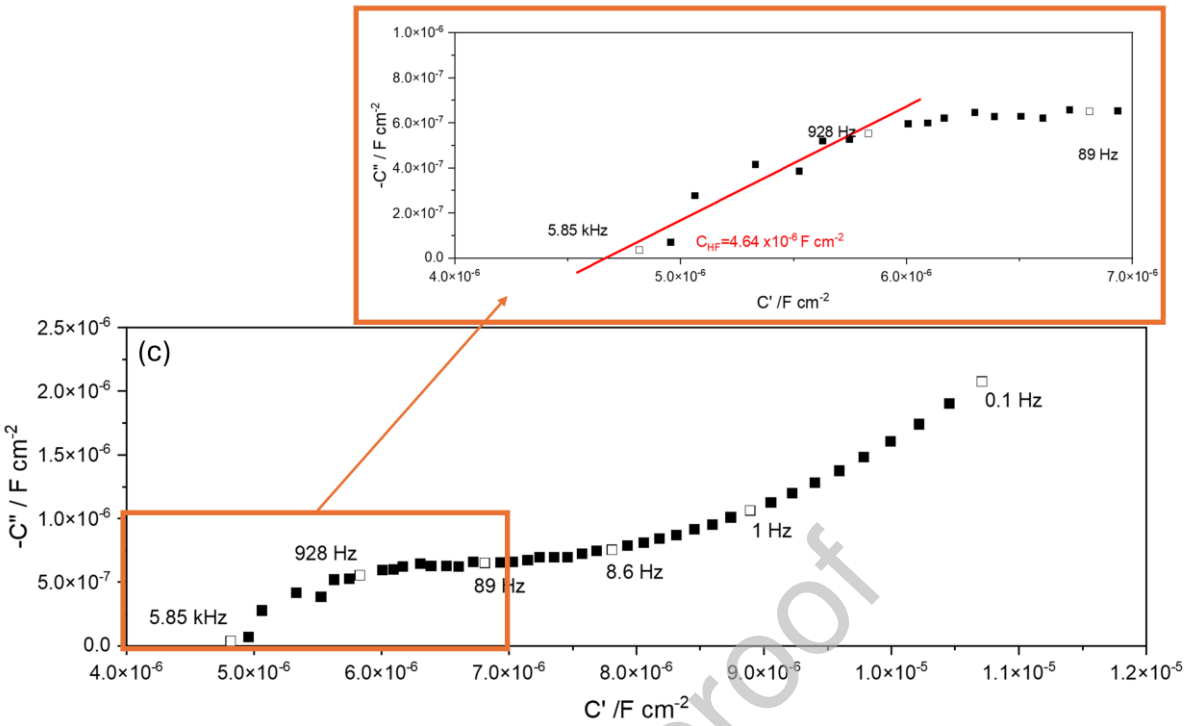

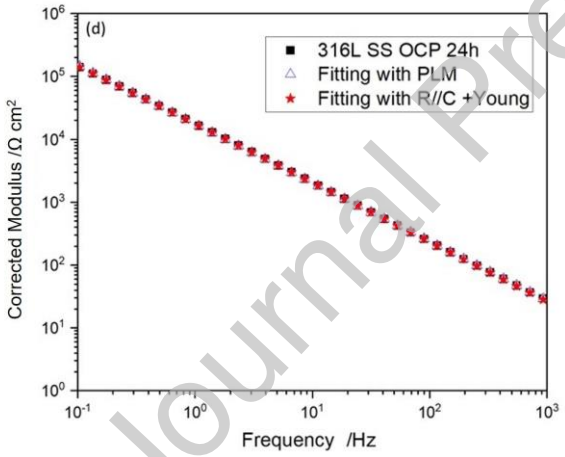

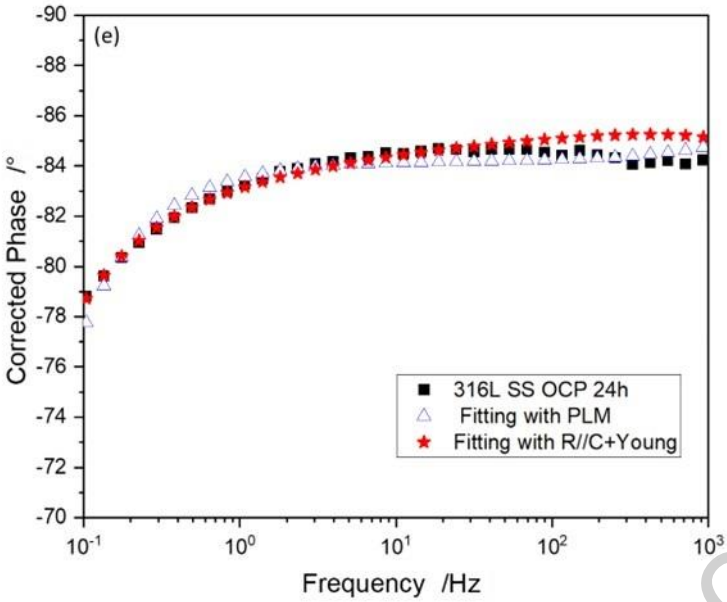

Figure 7. *Resistivity profiles through the passive film grown during 24h in aerated 0.05 M H_3BO_3 + 0.075 M $Na_2B_4O_7$ 10H_2O borate buffer solution (pH=9.2) on 316L stainless steel obtained by PLM (blue open triangle) and DBLM (red star). Dash lines represent the profiles accounting for the deviations on regressed parameters.*

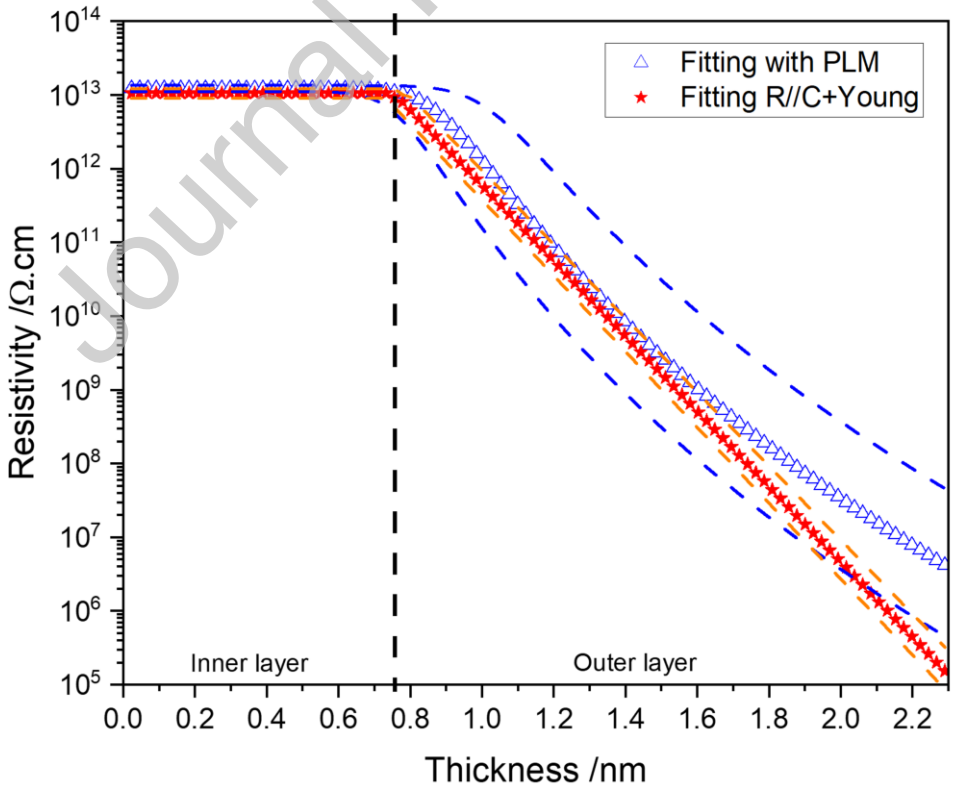

***Figure 8**. XPS high resolution Fe2p (a), Cr2p (b) and Ni2p (c) core level spectra, collected after sputtering times going from 30s to 2250s on passive film grown on 316L stainless steel after 24h in borate buffer solution.*

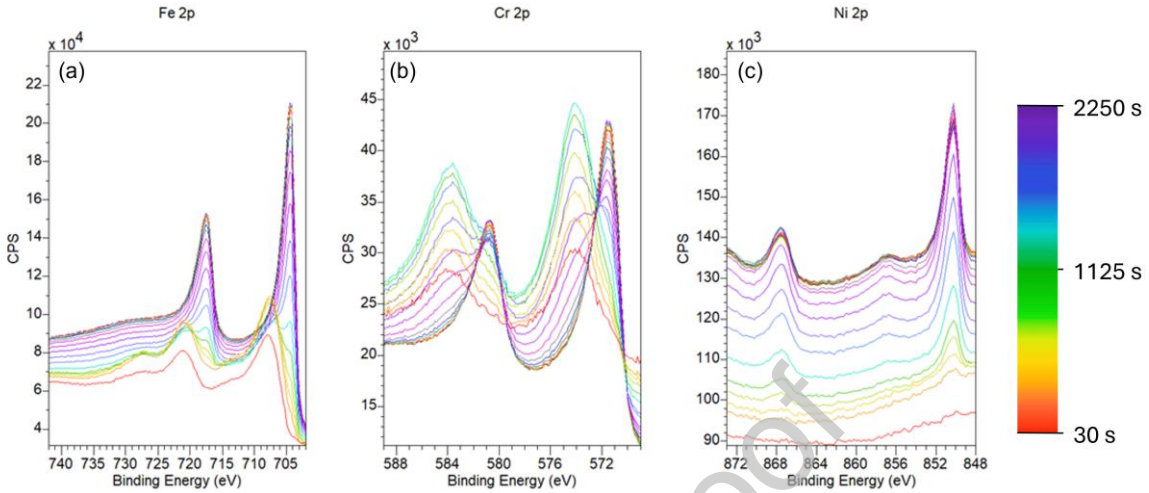

***Figure 9.** Composition of the passive film and the underneath layer for 316L stainless steel after 24h in a borate buffer solution obtained from XPS measurement: a) Raw and Modelled areas of XPS contributions; b) Atomic concentrations extracted from the multilayer model.*

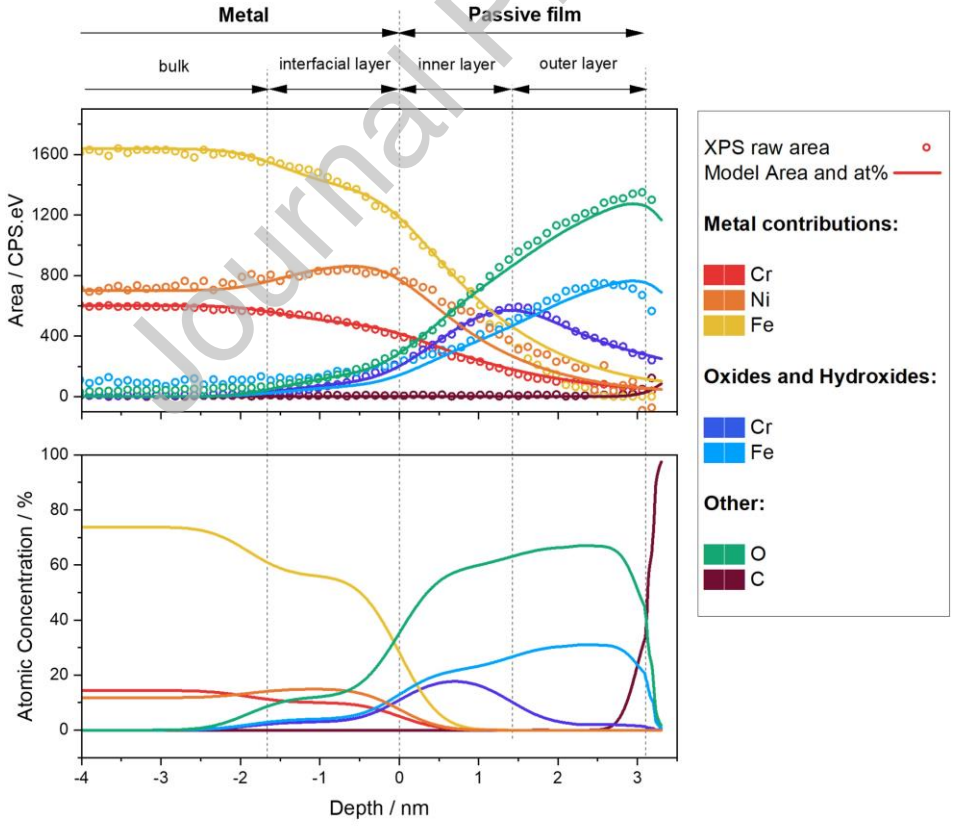

Table captions:

Table 1. *Four sets of Power Law Model parameters used for theoretical impedance response: Data 1, Data 2, Data 3, Data 4.*

Table 2. *Regression results using DBLM and calculated parameters for the different data set defined in Table 1. Confidence intervals are given for the regression and calculated parameters.*

Table 3. *Regression results using PLM (EEC 1) and DBLM (EEC 2) for 316L stainless steel after 24h in aerated 0.05 M H_3BO_3 + 0.075 M $Na_2B_4O_7$ 10H_2O borate buffer solution (pH=9.2). Confidence intervals are given for the regression parameters.*

Table 4. *Parameters from XPS spectra analysis: fitting parameters and average atomic chemical composition of the layers: bulk metal, modified metal layer, inner and outer layers of the passive film and contamination layer.*

Table 1

	Data 1	Data 2	Data 3	Data 4
α	0.95	0.95	0.9	0.85
ρ_0 (Ω cm)	10^{13}	10^{13}	10^{13}	10^{13}
ρ_δ (Ω cm)	10^{5}	10^{3}	10^{5}	10^{5}
δ (nm)	3	3	3	3
γ*	20	20	10	6.66
Q_{PLM} (μF $s^{(\alpha-1)}$ cm^{-2})**	7.9	9.9	17.4	38.1

* Calculated from Eq. 2; **Calculated from Eq. 8

Table 2

	Data 1	Data 2	Data 3	Data 4
ρ_0 (Ω cm)	1.0 10^{13}±1.10%	9.8 10^{12}±1.10%	1.2 10^{13}±4.50%	1.0 10^{13}±10.0%
δ_{in} (nm)	1.12 ±0.60%	0.88 ±0.76%	0.35 ±3.70%	0.13 ±15.0%
δ_{out} (nm)	1.80 ±0.05%	2.10 ±0.04%	2.64±0.16%	2.83 ±0.24%
λ (nm)	0.08 ±0.05%	0.07 ±0.04%	0.09 ±0.16%	0.07 ±0.26%
χ	0.99	1.00	4.20	9.32
$\rho_{\delta,calc}$ (Ω cm)*	8.2 10^{3} ±2.23%	4.4 10^{-1} ±2.30%	4.8 10^{0} ±9.20%	6.2 10^{-5} ±20.1%
δ_{tot} (nm)	2.92 ±0.26%	2.98 ±0.25%	2.99 ±0.57%	2.96 ±0.88%
R_{in} (Ω cm^2)**	1.1 10^{6} ±1.70%	8.8 10^{5} ±1.86%	3.5 10^{5} ±8.20%	1.3 10^{5} ±25.0%
C_{in} (μF cm^{-2})**	9.6 10^{-6} ±0.60%	1.2 10^{-5} ±0.76%	3.0 10^{-5} ±3.70%	8.2 10^{-5} ±15.0%

*Calculated from Eq. 3; **Calculated from Eqs. 10a and 10b; $\delta_{tot} = \delta_{in} + \delta_{out}$

Table 3

	Re (Ω cm^2)	**K**	**ρ_0 (Ω cm)**	**ρ_δ (Ω cm)***	**δ (nm)****	**α**	**χ**
Fit with EEC1	108.1 ±0.67%	$6.17\ 10^{-7}$ ±0.41%	$1.23\ 10^{13}$ ±9.8%	$4.19\ 10^{6}$ ±89.1%	2.30 ±11.3%	0.935 ±0.05%	0.78
	Re (Ω cm^2)	**δ_{in} (nm)**	**ρ_0 (Ω cm)**	**ρ_δ (Ω cm)*****	**δ_{out} (nm)**	**λ (nm)**	**χ**
Fit with EEC2	109.1 ±0.40%	0.76 ±0.40%	$1.06\ 10^{13}$ ±15.5%	$1.61\ 10^{5}$ ±22.7%	1.53 ±0.21%	0.085 ±0.28%	0.65

* Calculated from Eq. 14; ** Determined by graphical approach; *** Calculated from Eq. 3 while x=δ

Table 4

Layer	Thickness (nm)	Density (g cm^{-3})	roughness factor	Composition (at%)						
				Cr Met	Ni Met	Fe Met	Cr Ox	Fe Ox	O	C
Metal										
bulk	∞	8	4	14.4	11.8	73.8	0	0	0	0
interfacial	1.9	7.6	4	10	15	56	3	4	12	0
Passive Film										
Inner layer	1.4	5.8	4	0	0	0	19	22	59	0
Outer layer	1.7	5.6	2	0	0	0	2	31	67	0
Contamination layer	0.2	2	1	0	0	0	0	0	0	100

Declaration of interests

☒ The authors declare that they have no known competing financial interests or personal relationships that could have appeared to influence the work reported in this paper.

☐ The authors declare the following financial interests/personal relationships which may be considered as potential competing interests: